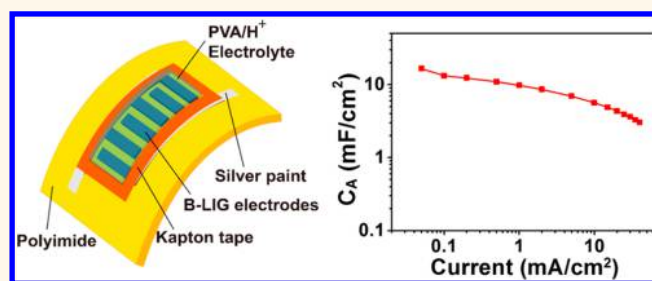


# Flexible Boron-Doped Laser-Induced Graphene Microsupercapacitors

Zhiwei Peng,<sup>†</sup> Ruquan Ye,<sup>†</sup> Jason A. Mann,<sup>†</sup> Dante Zakhidov,<sup>†</sup> Yilun Li,<sup>†</sup> Preston R. Smalley,<sup>†,‡</sup> Jian Lin,<sup>\*,§</sup> and James M. Tour<sup>\*,†,‡,§</sup>

<sup>†</sup>Department of Chemistry, <sup>‡</sup>Smalley Institute for Nanoscale Science and Technology, and <sup>§</sup>Department of Materials Science and NanoEngineering, Rice University, 6100 Main Street, Houston, Texas 77005, United States, <sup>‡</sup>Second Baptist School, 6410 Woodway Drive, Houston, Texas 77057, United States, and <sup>||</sup>Department of Mechanical & Aerospace Engineering, University of Missouri, Columbia, Missouri 65211, United States

**ABSTRACT** Heteroatom-doped graphene materials have been intensely studied as active electrodes in energy storage devices. Here, we demonstrate that boron-doped porous graphene can be prepared in ambient air using a facile laser induction process from boric acid containing polyimide sheets. At the same time, active electrodes can be patterned for flexible microsupercapacitors. As a result of boron doping, the highest areal capacitance of as-prepared devices reaches 16.5 mF/cm<sup>2</sup>, 3 times higher than nondoped devices, with concomitant energy density increases of 5–10 times at various power densities. The superb cyclability and mechanical flexibility of the device are well-maintained, showing great potential for future microelectronics made from this boron-doped laser-induced graphene material.



**KEYWORDS:** boron-doped · laser induction · graphene · microsupercapacitor · flexible · porous graphene · energy storage

Energy storage systems, such as supercapacitors (SCs) and lithium ion batteries (LIBs), have been widely studied over the past few years in order to meet the rapidly growing demand for highly efficient energy devices.<sup>1–5</sup> Intense ongoing research has focused on miniaturized portable electronics which require small size, light weight, and mechanical flexibility while maintaining high energy and power densities.<sup>6–9</sup> Recent progress in microfabrication technologies has allowed for the in-plane manufacturing of microsupercapacitors (MSCs) made using lithographic techniques that would be suitable for integrated circuits.<sup>10,11</sup> However, such fabrication methods may not be cost-effective for projected commodity targets, slowing their scalability and commercialization.

Graphene-based materials have been extensively studied as active electrodes in MSCs due to their unique structure and their extraordinary mechanical and electrical properties.<sup>12–16</sup> To further improve their performances, many methods have been employed to modulate the electronic band structure of the graphene-derived

materials.<sup>17–32</sup> Among them, doping with heteroatoms (such as boron, nitrogen, phosphorus, and sulfur) has been shown to be an effective way to tailor the electrochemical properties of graphene-derived conductive materials and to enhance their capacitive performances.<sup>24–32</sup> Particularly, substitutions of carbon with boron in the graphene lattice shifts the Fermi level toward the valence band, thereby enhancing charge storage and transfer within the doped graphene structure.<sup>29–32</sup> Moreover, the presence of boron dopants in graphene contributes to a space-charge-layer capacitance and/or pseudocapacitance, further increasing the apparent capacitance.<sup>33,34</sup> Despite its advantageous doping effect, the current synthesis processes for obtaining boron-doped graphene require either multistep chemical reactions<sup>28–31</sup> or high-temperature and high-vacuum environments,<sup>28,31,32</sup> making them unsuitable for low-cost commodity-driven applications. Recently, we described a simple and robust laser induction method to prepare porous graphene structures from commercially available polyimide (PI) sheets, and the as-made

\* Address correspondence to linjian@missouri.edu, tour@rice.edu.

Received for review January 20, 2015 and accepted May 15, 2015.

Published online 10.1021/acs.nano.5b00436

© XXXX American Chemical Society

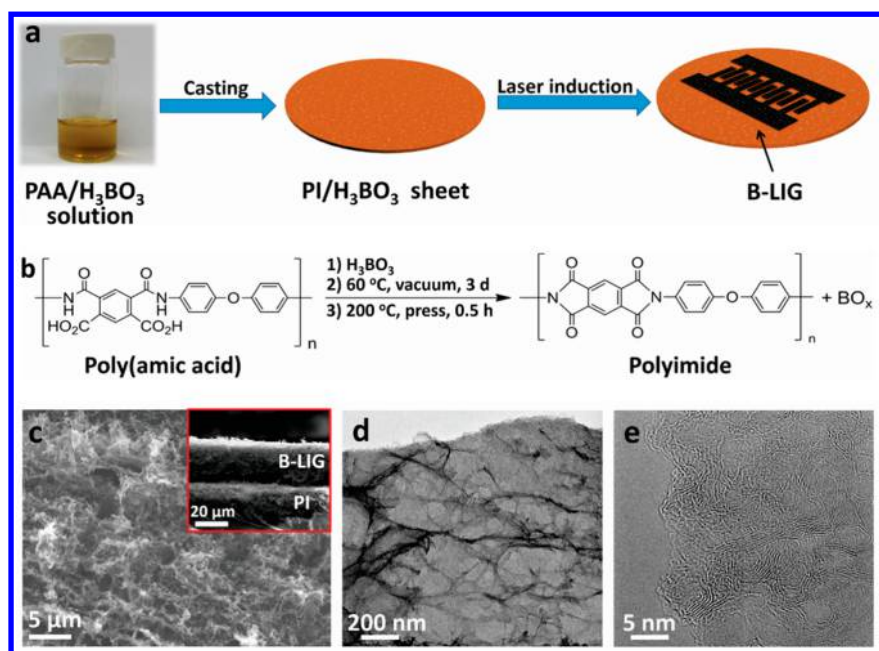


**Figure 1.** (a) Synthetic scheme for the preparation of B-LIG and fabrication of the B-LIG-MSC. (b) Scheme of the dehydration reaction from PAA to a PI film during the curing process. (c) SEM images of 5B-LIG. The inset in (c) is the cross sectional SEM image of 5B-LIG on a PI sheet. (d) TEM image of 5B-LIG. (e) HRTEM image of 5B-LIG.

laser-induced graphene (LIG) showed promising electrochemical performance.<sup>35,36</sup>

Here, we report that boron-doped LIG (B-LIG) can be synthesized with a similar laser induction method that is performed in air using a standard commercial laser writing tool as found in common machine shops. The synthesis starts by dissolving H<sub>3</sub>BO<sub>3</sub> into poly(pyromellitic dianhydride-co-4,4'-oxydianiline amic acid) (or poly(amic acid), PAA) solution as a boron precursor, followed by condensation of the PAA to produce a boric-acid-containing PI sheet. Subsequent laser induction using a commercial CO<sub>2</sub> laser writes patterns on the as-prepared PI sheet under ambient conditions. During the laser induction, the surface of the PI sheet, with its H<sub>3</sub>BO<sub>3</sub>, transforms into B-LIG. At the same time, the B-LIG on the PI film can be patterned into interdigitated shapes for flexible MSCs. The resulting B-LIG has significantly improved electrochemical performance over the nondoped structures, with 3 times higher capacitance and 5–10 times higher energy density than we achieved in pristine boron-free samples.<sup>36</sup> The transformation of PAA to PI is essential for the successful formation of LIG with high electrochemical properties. Meanwhile, the cyclability and flexibility of as-prepared devices are well-maintained, demonstrating the potential of B-LIG materials for future low-cost energy storage devices. Compared to other common boron-doping methods, the laser induction process at room temperature and ambient air presented here is much simpler and more cost-effective, and the synthesized B-LIG material might also be applied in other applications such as metal-free oxygen reduction reaction

catalyst,<sup>29</sup> solar cells,<sup>37</sup> field emission transistors,<sup>38</sup> and lithium ion batteries.<sup>39</sup>

## RESULTS AND DISCUSSION

Figure 1a shows a scheme for the synthesis and patterning process of B-LIG materials for MSCs. Starting with a 12.8 wt % PAA solution in *N*-methylpyrrolidone, various weight percentages of H<sub>3</sub>BO<sub>3</sub> (0, 1, 2, 5, and 8 wt % relative to PAA) were added and mixed under bath sonication for 30 min to form a uniform precursor solution. Next, the solution was poured into an aluminum dish and the solvent removed in a vacuum oven at 60 °C for 3 days, resulting in a solid PAA/H<sub>3</sub>BO<sub>3</sub> sheet. The PAA/H<sub>3</sub>BO<sub>3</sub> sheet was then placed in a hydraulic press (Carver press) and heated to 200 °C for 30 min under a pressure of ~0.3 MPa to dehydrate the PAA/H<sub>3</sub>BO<sub>3</sub> sheet and form the PI/H<sub>3</sub>BO<sub>3</sub> film.<sup>40</sup> During this step, PAA and H<sub>3</sub>BO<sub>3</sub> will dehydrate and transform into PI and BO<sub>x</sub>, as shown in Figure 1b. The successful transformation from PAA to PI was also confirmed by the FT-IR measurement as shown in Supporting Information Figure S1. In the spectrum from the PI sheet, the C–N amide band at 1542 cm<sup>−1</sup> disappeared, while the characteristic absorption bands of imide groups near 1778, 1724, 1377, and 721 cm<sup>−1</sup> were present.<sup>41</sup> The dehydration from PAA to PI is crucial for successful formation of LIG and will be discussed in detail below. Finally, a standard CO<sub>2</sub> laser cutting system was used under ambient conditions to convert PI/H<sub>3</sub>BO<sub>3</sub> to xB-LIG (*x* = 0, 1, 2, 5, and 8, which denotes the initial H<sub>3</sub>BO<sub>3</sub> loading weight percentages).<sup>35,36</sup> Optical images of the PAA/H<sub>3</sub>BO<sub>3</sub> solution and patterned B-LIG on a PI/H<sub>3</sub>BO<sub>3</sub> sheet are presented in Figure S2.

More details can be found in the Methods section. Here, the incorporation of  $\text{H}_3\text{BO}_3$  into the PAA was essential. Attempts to incorporate boron from sources other than  $\text{H}_3\text{BO}_3$ , including ammonia borane and *m*-carborane, resulted in little or no boron doping of the LIG. This is likely because boric acid dehydrates and polymerizes on heating while the other two evaporate or sublime, causing the failure of boron doping. The major advantage of this synthetic process is that B-LIG can be fabricated and patterned at the same time during laser induction, making it an ideal material for future roll-to-roll processing.

The morphology of formed B-LIG was characterized using scanning electron microscopy (SEM) and transmission electron microscopy (TEM). Figure 1c shows an SEM image of the as-prepared 5B-LIG that exhibits a porous structure due to the rapid formation of gaseous products during laser induction. The inset in Figure 1c reveals that the thickness of 5B-LIG on the PI sheet surface is  $\sim 25\ \mu\text{m}$ . The thickness of B-LIG is uniform over the entire high-exposed distance (Figure S3) and independent of initial  $\text{H}_3\text{BO}_3$  loadings (Figure S4). SEM EDAX elemental mapping is also present in Figure S5 to show that carbon, boron, and oxygen were homogeneously distributed within the 5B-LIG sample. Figure 1d shows the TEM image of 5B-LIG at low magnification containing few-layer graphene structures with nanoscale ridges and wrinkles, which would be beneficial for higher accessible surface area and therefore enhanced electrochemical performance.<sup>42</sup> High-resolution TEM (HRTEM) image in Figure 1e and Figure S6 further confirms the graphitic nature of the 5B-LIG nanosheet. Numerous graphene edges were found on the surface of the 5B-LIG nanosheets, which is similar to our previous study on LIG,<sup>34</sup> again indicating a highly accessible surface area. For comparison, LIG materials with different loadings of  $\text{H}_3\text{BO}_3$  (0B-LIG, 1B-LIG, 2B-LIG, and 8B-LIG) were also prepared and imaged with SEM and TEM (Figures S7 and S8). No significant difference was found among these samples, indicating that the loading of  $\text{H}_3\text{BO}_3$  has little effect on the morphology of the resulting B-doped LIG.

Raman spectroscopy and powder X-ray diffraction (XRD) were further used to characterize the morphology of the B-LIG material. The Raman spectrum of 5B-LIG in Figure 2a shows three characteristic peaks for graphene-derived material: the D peak at  $\sim 1350\ \text{cm}^{-1}$  induced by defects or disordered bent sites,<sup>43</sup> the G peak at  $\sim 1590\ \text{cm}^{-1}$  showing graphitic  $\text{sp}^2$  carbon, and the 2D peak at  $\sim 2700\ \text{cm}^{-1}$  originating from second-order zone boundary phonons.<sup>44,45</sup> The large D peak observed here could arise from numerous graphene edges, consistent with our observations by TEM (Figure 1e), boron doping into the LIG sheets, or the bending of the graphene layers in the porous structure.<sup>43</sup> The XRD pattern in Figure 2b shows a prominent peak at  $2\theta = 26^\circ$ , indicating an interlayer

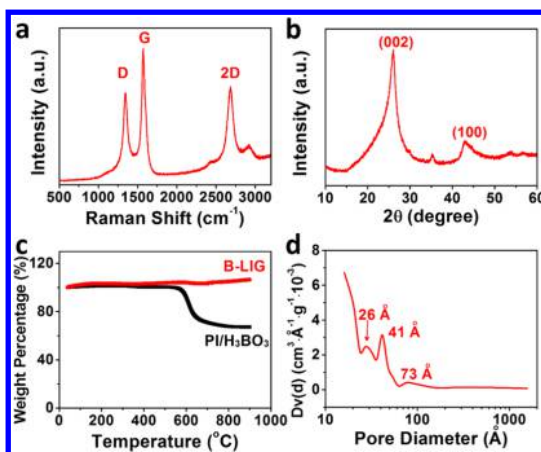


Figure 2. Characterization of 5B-LIG material. (a) Raman spectrum of 5B-LIG. (b) XRD pattern of 5B-LIG. (c) TGA curve of 5B-LIG and 5B-PI,  $5^\circ\text{C}/\text{min}$  under argon. (d) Pore size distribution of 5B-LIG.

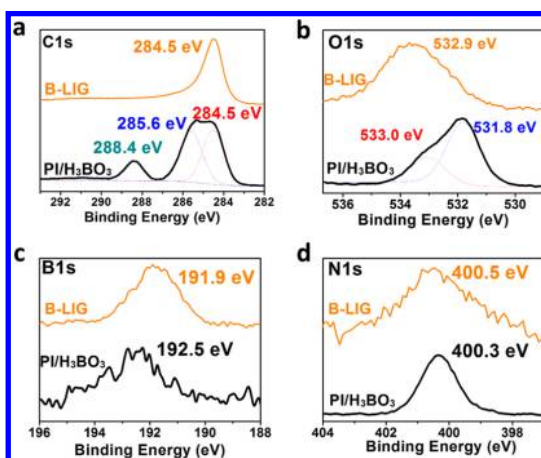
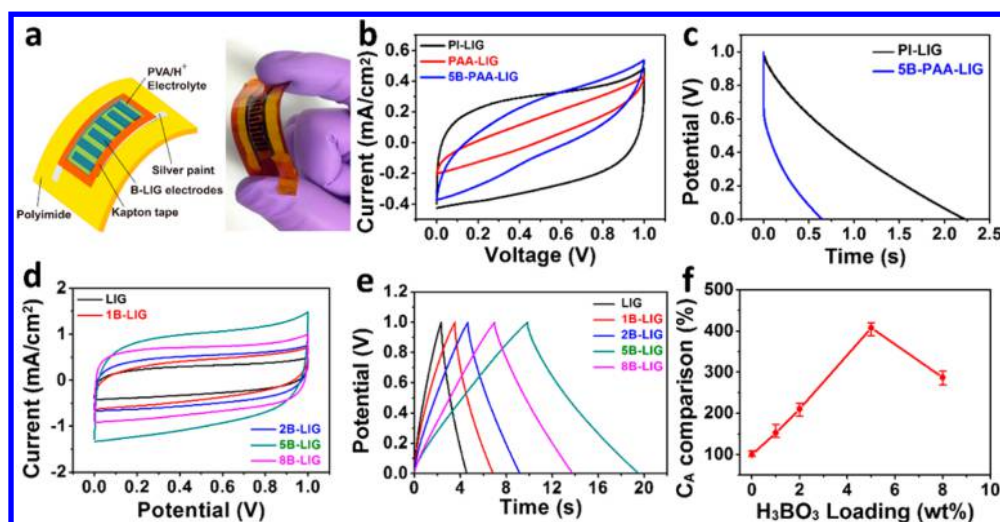


Figure 3. XPS spectra of 5B-LIG and  $\text{PI}/\text{H}_3\text{BO}_3$  sheet. (a) C 1s spectrum. (b) O 1s spectrum. (c) B 1s spectrum. (d) N 1s spectrum.

spacing of  $\sim 3.4\ \text{\AA}$  between (002) graphitic crystal planes in 5B-LIG. A (100) graphitic crystal phase was also found at  $2\theta = 43^\circ$ . The high degree of graphitization of 5B-LIG is also verified by thermogravimetric analysis (TGA) measurement under argon (Figure 2c). The  $\text{PI}/\text{H}_3\text{BO}_3$  substrate begins to decompose at  $550^\circ\text{C}$ , whereas 5B-LIG remains stable over  $900^\circ\text{C}$ . From BET analysis (Figure S9), the surface area of 5B-LIG is  $191\ \text{m}^2/\text{g}$ . Figure 2d shows the pore size distributions of 5B-LIG, which are all  $<10\ \text{nm}$  (26, 41, and  $73\ \text{\AA}$ ).

To confirm the boron doping in the product, X-ray photoelectron spectroscopy (XPS) was performed on a  $\text{H}_3\text{BO}_3$ -loaded sample before and after laser induction, as shown in Figure S10 for survey spectra and Figure 3 for elemental spectra. Prior to laser induction, the C 1s peak originating from  $\text{PI}/\text{H}_3\text{BO}_3$  could be fitted by three subpeaks: 284.5, 285.6, and  $288.4\ \text{eV}$ , representing C–C, C–N, and C–O–C=O bonding, respectively (Figure 3a).<sup>46</sup> For the O 1s peak, two subpeaks can be found at 533.0 and  $531.8\ \text{eV}$ , representing C–O and



**Figure 4.** Electrochemical performance comparison of LIG-MSCs with different  $\text{H}_3\text{BO}_3$  loadings. (a) Schematic of a B-LIG-MSC device and the digital photograph of a fully fabricated device under bending. (b) CV curves of MSCs from PI-derived LIG, PAA-derived LIG, and PAA/ $\text{H}_3\text{BO}_3$ -derived LIG at a scan rate of 0.1 V/s. (c) CC curves of MSCs from PI-derived LIG and PAA/ $\text{H}_3\text{BO}_3$ -derived LIG at a current density of 1.0  $\text{mA}/\text{cm}^2$ . (d) CV curves of LIG-MSC and B-LIG-MSC with different  $\text{H}_3\text{BO}_3$  loadings. The scan rate is set at 0.1 V/s. (e) Galvanostatic CC curves of LIG-MSC and B-LIG-MSC with different  $\text{H}_3\text{BO}_3$  loadings. The current density is set at 1  $\text{mA}/\text{cm}^2$ . (f) Comparison of calculated  $C_A$  from LIG-MSC and B-LIG-MSC with different  $\text{H}_3\text{BO}_3$  loadings. Current density is 1  $\text{mA}/\text{cm}^2$ . At least three devices were tested for each xB-LIG sample.

$\text{C}=\text{O}$  bonding (Figure 3b).<sup>47</sup> After laser induction, the 5B-LIG only showed a single prominent peak at 284.5 eV for C 1s and 532.9 eV for O 1s, and the atomic percentage of carbon increased from 72 to 84%, whereas oxygen decreased from 19 to 4.3%, indicating that the imide group containing  $\text{C}=\text{O}$  bonding forms a graphitic structure. Also, the B 1s peak (Figure 3c) shifted from 192.5 eV in B-PI down to 191.9 eV in 5B-LIG after laser induction, showing that boron in the LIG sheet was in the form of  $\text{B}-\text{N}$ ,  $\text{BCO}_2$ , or  $\text{BC}_2$ .<sup>27,28,30,48</sup> The position of N 1s changed little after laser treatment (Figure 3d), but its atomic percentage dropped from 7.6 to 2.0%, again indicating that the imide group is the main reacting site during the laser induction process.

To investigate the electrochemical properties of the B-LIG, it was directly patterned into interdigitated electrodes during laser induction and then fabricated into in-plane MSCs, as shown in Figure 4a. Note that the laser induction patterning process for a device with a size shown in Figure S2b is done in <3 min at room temperature and ambient atmosphere. A solid-state electrolyte made from poly(vinyl alcohol) (PVA) and  $\text{H}_2\text{SO}_4$  was used to ensure the flexibility of the device. Our previous study also showed that polymeric electrolytes promote a better electrochemical performance from LIG than conventional aqueous electrolytes.<sup>36</sup> To demonstrate the importance of the dehydration reaction of PAA to PI, PAA sheets with or without  $\text{H}_3\text{BO}_3$  were directly laser-induced and fabricated into MSC to first compare their electrochemical performance. Cyclic voltammetry (CV) and charge–discharge (CC) measurements of corresponding MSC devices are exhibited and compared in Figure 4b,c. Both PAA-derived LIG-MSC and boron-doped PAA-derived

LIG-MSC showed smaller and tilted CV curves compared to those of boron-free PI-derived LIG-MSC in Figure 4b, representing a lower capacitance and a higher resistance. The large voltage drop observed at the initial stage of discharge run in PAA-derived LIG-MSC from Figure 4c also indicates a higher internal resistance. This result shows that the dehydration step from PAA to PI is crucial for successful formation of B-LIG with higher quality and better electrical conductivity.

We compare the electrochemical performance of B-LIG with different initial  $\text{H}_3\text{BO}_3$  loadings. At a scan rate of 0.1 V/s, all CV curves from xB-LIG-MSCs ( $x = 0, 1, 2, 5$ , and 8) are pseudorectangular, as shown in Figure 4d, representing good electrochemical double-layer (EDL) character.<sup>23,35,36</sup> Among them, 5B-LIG-MSC shows the largest areal capacitance ( $C_A$ ), as evidenced by its highest CV current. From Figure 4e, all galvanostatic CC curves from B-LIG-MSCs at a current density of 1  $\text{mA}/\text{cm}^2$  show a nearly triangular shape, further confirming the good capacitive behavior of the devices. Again, 5B-LIG-MSC exhibits the longest discharge runtime, indicating the best capacitance performance. Figure 4f shows the influence of boron content on  $C_A$ , which increases from 0 to 5%, reaching a maximum  $\sim 4$  times greater than undoped LIG, and then decreases slightly at higher loadings. The relationship between the initial  $\text{H}_3\text{BO}_3$  loading amount and the resulting B content in xB-LIG samples and their respective capacitances is summarized in Table S1. When the boron-doping level is low, increasing boron dopants into LIG will increase the hole charge density, thus enhancing the electrons' charge storage.<sup>30–32</sup> However, after a saturation threshold, additional boron



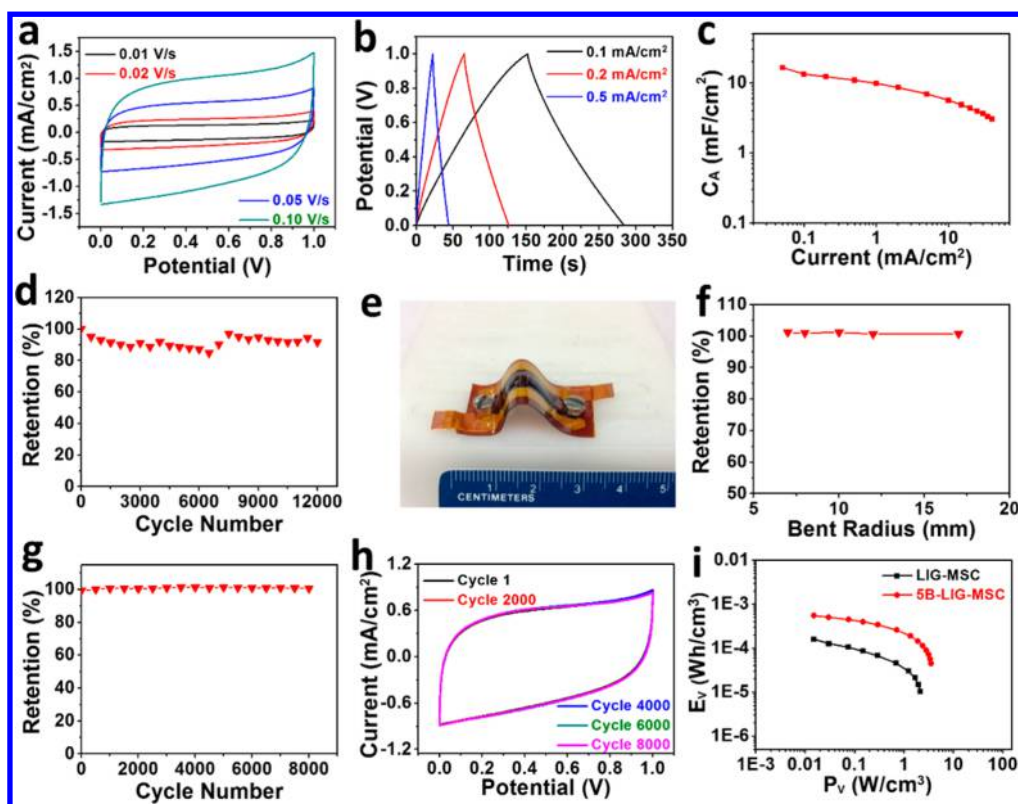


Figure 5. Electrochemical performance of 5B-LIG-MSC. (a) CV curves of 5B-LIG-MSC at scan rates of 10, 20, 50, and 100 mV/s. (b) Galvanostatic CC curves of 5B-LIG-MSC at current densities of 0.1, 0.2, and 0.5 mA/cm<sup>2</sup>. (c)  $C_A$  of 5B-LIG-MSC calculated from CC curves as a function of current density. (d) Cyclability testing of 5B-LIG-MSC. The charge–discharge cycles are performed at a current density of 1.0 mA/cm<sup>2</sup>. (e) Digital photograph of a bent 5B-LIG-MSC at a bending radius of 10 mm. (f) Capacitance retention of 5B-LIG-MSC at different bending radii. (g) Bent cyclability testing of flexible 5B-LIG-MSC at a fixed bending radius of  $\sim 10$  mm. The  $C_p$  is calculated from discharge runtime at a current density of 1.0 mA/cm<sup>2</sup>. (h) CV curves of the 5B-LIG-MSC at different bending cycles in (g) at a scan rate of 50 mV/s. (i) Volumetric Ragone plot of 5B-LIG-MSC and LIG-MSC.

doping might induce more scattering sites for electrons in the LIG sheet, lowering the conductivity of the material, causing the decrease of  $C_A$ .<sup>49</sup> In addition, higher H<sub>3</sub>BO<sub>3</sub> loadings could inhibit the dehydration process of PAA, resulting in the retardation of efficient PI formation. As a result, an optimum content of H<sub>3</sub>BO<sub>3</sub> is needed to maximize the device performance.

Because 5B-LIG-MSC shows the highest  $C_A$  among different H<sub>3</sub>BO<sub>3</sub> loading samples, it was chosen to further examine the electrochemical performance of the 5B-LIG-MSC. Figure 5a shows CV curves of a 5B-LIG-MSC at scan rates of 0.01, 0.02, 0.05, and 0.10 V/s. The maintained pseudorectangular shape of the CV curves over different scan rates represents good EDL formation of the devices. Figure 5b shows the galvanostatic CC curves at different current densities (0.1, 0.2, and 0.5 mA/cm<sup>2</sup>), all of which are nearly triangular, further confirming their excellent capacitive behaviors. Additional CV curves at higher scan rates and CC curves at higher current densities are shown in Figure S11 to demonstrate that 5B-LIG-MSC can operate over a wide range of scan rates and current densities. The  $C_A$  determined from these CC curves shows little decrease over current densities covering 2 orders of magnitude,

with a maximum of 16.5 mF/cm<sup>2</sup> at a current density of 0.05 mA/cm<sup>2</sup>, which is 4 times larger than that of the nondoped LIG made from the same process without H<sub>3</sub>BO<sub>3</sub> incorporated. Furthermore,  $C_A$  of 5B-LIG-MSC remains over 3 mF/cm<sup>2</sup> even when operated at a high current density of 40 mA/cm<sup>2</sup>, indicating excellent power performance. For better evaluation, volumetric capacitances of 5B-LIG-MSC over different current densities are also provided in Figure S12. Table S2 summarizes the electrochemical performances of various MSCs from literature and comparison with current work. Electrochemical impedance measurements shown in Figure S13 further demonstrate that both external and internal resistances of 5B-LIG-MSC are lower than that of LIG-MSC. These results indicate faster ionic transport and possibly better electrode–electrolyte interface when the LIG material is doped with boron. The cyclability of 5B-LIG-MSCs was also tested over 12,000 CC cycles at a current density of 1.0 mA/cm<sup>2</sup> with over 90% of the capacitance retained (Figure 5d) and an almost unchanged CV curve shape (Figure S14), proving high stability of performance from the B-LIG-MSC. The capacitance increase during the cycling test could come from the osmosis of

electrolyte through the layers of 5B-LIG, creating more accessible surface area for the formation of the EDL structure.<sup>26,29,31,53</sup>

In addition to high  $C_A$ , the assembled MSC from 5B-LIG also shows excellent durability under mechanical stress. When the device was bent and fixed (Figure 5e) at different bending radii (from 7 to 17 mm), the calculated  $C_A$  from discharge runtime remained essentially constant, as shown in Figure 5f. Furthermore, after 8000 bending cycles at a radius of 10 mm, the  $C_A$  of the device was unchanged (Figure 5g), and CV curves during different bending cycles, as shown in Figure 5h, are identical to each other, suggesting that bending had little effect on the electrochemical performance of 5B-LIG-MSC. To further demonstrate the high capability of 5B-LIG-MSC over nondoped devices, a Ragone plot of volumetric power density ( $P_V$ ) versus energy density ( $E_V$ ) was compared and is shown in Figure 5i by using the entire area of the devices including the gaps between the electrodes and the electrode thickness. Under different  $P_V$ , the  $E_V$  of 5B-LIG-MSC was 5–10 times larger than that of LIG-MSC without boron doping. To better evaluate its commercial potential, Ragone plots of 5B-LIG-MSC with specific areal and volumetric energy density and power density calculated from the electrode area of the devices are also provided

in Figure S15. The remarkable electrochemical performance, cyclability over charge–discharge times, and stability under bending makes B-LIG a promising candidate as an energy storage unit for next-generation flexible and portable electronics.

## CONCLUSION

In summary, we have reported a facile and robust laser induction process to prepare boron-doped graphene structures from polyimide films, which can be used as an active material for flexible in-plane micro-supercapacitors. With boron doping, the electrochemical performance of B-LIG is enhanced with 3 times larger areal capacitance and 5–10 times larger volumetric energy density at various power densities. Also, the transformation of PAA to PI is proven to be crucial for the successful formation of LIG with high quality and good electrochemical property. Meanwhile, the cyclability and flexibility of the as-prepared device is well-maintained. Considering the simplicity of material synthesis in ambient air and the easy device fabrication, boron-doped LIG materials hold promise for energy storage devices in portable microelectronics. The laser induction method may also open up a new avenue for the facile synthesis of boron-doped graphene materials and their use in varied applications.

## METHODS

**Materials Synthesis and Device Fabrication.** PAA solution (7.8 g, 12.8 wt %, 575798-250 ML, Sigma-Aldrich) was used as the precursor solution for formation of a polyimide sheet. Various amounts of  $H_3BO_3$  (B0394, Aldrich) (10 mg for 1 wt %, 20 mg for 2 wt %, 50 mg for 5 wt %, and 80 mg for 8 wt %) were added to the PAA solution with bath sonication for 30 min and then poured into an aluminum dish and placed in a vacuum oven at 60 °C and a pressure of  $\sim 120$  mmHg for 3 days to evaporate the solvent. The filming process was done in a hydraulic press (Carver, No. 3912) with an applied load of  $3 \times 10^5$  Pa at 200 °C for 30 min to dehydrate the PAA/ $H_3BO_3$  and form the PI/ $H_3BO_3$  sheet. Laser induction was then conducted on the PI/ $H_3BO_3$  substrate with a 10.6  $\mu$ m carbon dioxide ( $CO_2$ ) laser cutting system (Universal X-660 laser cutter platform at a pulse duration of  $\sim 14$   $\mu$ s and a spot size of  $\sim 120$   $\mu$ m). The laser power was fixed at 4.8 W, and the laser scan rate was set at  $\sim 8.9$  cm/s. The pulses per inch was set at 1000, and the image quality level was set at 6 for all experiments. All experiments were performed under ambient conditions. To fabricate in-plane MSCs, LIG was patterned into 12 interdigitated electrodes with a length of 5 mm, a width of 1 mm, and a spacing of  $\sim 300$   $\mu$ m between two neighboring microelectrodes. After that, Pellico colloidal silver paint (No. 16034, Ted Pella) was first applied on the common areas of both electrodes for better electrical contact. The electrodes were then extended with conductive copper tape, which was connected to an electrochemical workstation (CHI608D, CHI Instruments) for testing. A Kapton polyimide tape was employed to protect the common areas of the electrodes from electrolyte. Polymer electrolyte was made by stirring 10 mL of DI water, 1 mL of sulfuric acid (98%, Sigma-Aldrich), and 1 g of poly(vinyl alcohol) ( $M_w = 50\,000$ , Aldrich No. 34158-4) at 80 °C overnight. For the MSC device,  $\sim 0.25$  mL of electrolyte was dropped onto the active B-LIG area on the PI substrate and the device placed overnight in a desiccator that was connected to a house vacuum ( $\sim 120$  mmHg) to remove excess water.

**Characterization.** SEM images were obtained on a FEI Quanta 400 high-resolution field emission SEM. TEM and HRTEM images were obtained using a JEOL 2100F field emission gun transmission electron microscope. TEM samples were prepared by peeling off 5B-LIG from a PI substrate, followed by sonicating them in chloroform and dropping them onto a lacey carbon copper grid. Raman spectra were recorded on a Renishaw Raman microscope using a 514 nm laser with a power of 5 mW. XRD was conducted on a Rigaku D/Max Ultima II with Cu K $\alpha$  radiation ( $\lambda = 1.54$  Å). The surface area of 5B-LIG was measured with a Quantachrome Autosorb-3b BET surface analyzer. TGA (Q50, TA Instruments) was carried out from room temperature to 900 °C at 5 °C/min under argon flow. XPS was performed using a PHI Quantera SXM scanning X-ray microprobe with a base pressure of  $5 \times 10^{-9}$  Torr. Survey spectra were recorded in 0.5 eV step size with a pass energy of 140 eV. Elemental spectra were recorded in 0.1 eV step sizes with a pass energy of 26 eV. All the spectra were corrected using C 1s peaks (284.5 eV) as references. CV and galvanostatic CC measurements were performed using a CHI 608D workstation (USA). For the bending experiment, the device was fixed on a platform by two screws at different distances in which the bending radius can be calculated by the screw distance and the curved height of the device (Scheme S1). All of the measurements were conducted under ambient conditions.

**Conflict of Interest:** The authors declare no competing financial interest.

**Supporting Information Available:** Images, spectra, and additional calculation methods. The Supporting Information is available free of charge on the ACS Publications website at DOI: 10.1021/acsnano.5b00436.

**Acknowledgment.** This work was funded by the AFOSR (FA9550-09-1-0581) and the AFOSR MURI program (FA9550-12-1-0035). J.L. acknowledges support from the University of Missouri—Columbia (MU) and the MU Research Council.

## REFERENCES AND NOTES

- Liu, C.; Li, F.; Ma, L. P.; Cheng, H. M. Advanced Materials for Energy Storage. *Adv. Mater.* **2010**, *22*, E28–E62.
- Aricò, A. S.; Bruce, P.; Scrosati, B.; Tarascon, J.-M.; Van Schalkwijk, W. Nanostructured Materials for Advanced Energy Conversion and Storage Devices. *Nat. Mater.* **2005**, *4*, 366–377.
- Heon, M.; Lofland, S.; Applegate, J.; Nolte, R.; Cortes, E.; Hettinger, J. D.; Taberna, P.-L.; Simon, P.; Huang, P.; Brunet, M. Continuous Carbide-Derived Carbon Films with High Volumetric Capacitance. *Energy Environ. Sci.* **2010**, *4*, 135–138.
- Pech, D.; Brunet, M.; Taberna, P.-L.; Simon, P.; Fabre, N.; Mesnilgrete, F.; Conédéra, V.; Durou, H. Elaboration of a Microstructured Inkjet-Printed Carbon Electrochemical Capacitor. *J. Power Sources* **2010**, *195*, 1266–1269.
- Chen, W.; Beidaghi, M.; Penmatsa, V.; Bechtold, K.; Kumari, L.; Li, W.; Wang, C. Integration of Carbon Nanotubes to C-MEMS for On-Chip Supercapacitors. *IEEE Trans. Nanotechnol.* **2010**, *9*, 734–740.
- Pech, D.; Brunet, M.; Durou, H.; Huang, P.; Mochalin, V.; Gogotsi, Y.; Taberna, P.-L.; Simon, P. Ultrahigh-Power Micrometre-Sized Supercapacitors Based on Onion-like Carbon. *Nat. Nanotechnol.* **2010**, *5*, 651–654.
- Bae, J.; Song, M. K.; Park, Y. J.; Kim, J. M.; Liu, M.; Wang, Z. L. Fiber Supercapacitors Made of Nanowire-Fiber Hybrid Structures for Wearable/Flexible Energy Storage. *Angew. Chem., Int. Ed.* **2011**, *50*, 1683–1687.
- Pandolfo, A.; Hollenkamp, A. Carbon Properties and Their Role in Supercapacitors. *J. Power Sources* **2006**, *157*, 11–27.
- Wang, G.; Zhang, L.; Zhang, J. A Review of Electrode Materials for Electrochemical Supercapacitors. *Chem. Soc. Rev.* **2012**, *41*, 797–828.
- Kim, M. S.; Hsia, B.; Carraro, C.; Maboudian, R. Flexible Micro-supercapacitors with High Energy Density from Simple Transfer of Photoresist-Derived Porous Carbon Electrodes. *Carbon* **2014**, *74*, 163–169.
- Beidaghi, M.; Gogotsi, Y. Capacitive Energy Storage in Micro-scale Devices: Recent Advances in Design and Fabrication of Micro-supercapacitors. *Energy Environ. Sci.* **2014**, *7*, 867–884.
- Sun, Y.; Wu, Q.; Shi, G. Graphene Based New Energy Materials. *Energy Environ. Sci.* **2011**, *4*, 1113–1132.
- Dai, L. Functionalization of Graphene for Efficient Energy Conversion and Storage. *Acc. Chem. Res.* **2012**, *46*, 31–42.
- Xia, J.; Chen, F.; Li, J.; Tao, N. Measurement of the Quantum Capacitance of Graphene. *Nat. Nanotechnol.* **2009**, *4*, 505–509.
- El-Kady, M. F.; Kaner, R. B. Scalable Fabrication of High-Power Graphene Micro-supercapacitors for Flexible and On-Chip Energy Storage. *Nat. Commun.* **2013**, *4*, 1475.
- El-Kady, M. F.; Strong, V.; Dubin, S.; Kaner, R. B. Laser Scribing of High-Performance and Flexible Graphene-Based Electrochemical Capacitors. *Science* **2012**, *335*, 1326–1330.
- Zhu, Y.; Murali, S.; Stoller, M. D.; Ganesh, K.; Cai, W.; Ferreira, P. J.; Pirkle, A.; Wallace, R. M.; Cychosz, K. A.; Thommes, M. Carbon-Based Supercapacitors Produced by Activation of Graphene. *Science* **2011**, *332*, 1537–1541.
- Chen, S.; Zhu, J.; Wu, X.; Han, Q.; Wang, X. Graphene Oxide-MnO<sub>2</sub> Nanocomposites for Supercapacitors. *ACS Nano* **2010**, *4*, 2822–2830.
- Zhu, Y.; Li, L.; Zhang, C.; Casillas, G.; Sun, Z.; Yan, Z.; Ruan, G.; Peng, Z.; Raji, A.-R. O.; Kittrell, C. A Seamless Three-Dimensional Carbon Nanotube Graphene Hybrid Material. *Nat. Commun.* **2012**, *3*, 1225.
- Wen, Z.; Wang, X.; Mao, S.; Bo, Z.; Kim, H.; Cui, S.; Lu, G.; Feng, X.; Chen, J. Crumpled Nitrogen-Doped Graphene Nanosheets with Ultrahigh Pore Volume for High-Performance Supercapacitor. *Adv. Mater.* **2012**, *24*, 5610–5616.
- Liu, C.-L.; Chang, K.-H.; Hu, C.-C.; Wen, W.-C. Microwave-Assisted Hydrothermal Synthesis of Mn<sub>3</sub>O<sub>4</sub>/Reduced Graphene Oxide Composites for High Power Supercapacitors. *J. Power Sources* **2012**, *217*, 184–192.
- Zhang, C.; Peng, Z.; Lin, J.; Zhu, Y.; Ruan, G.; Hwang, C.-C.; Lu, W.; Hauge, R. H.; Tour, J. M. Splitting of a Vertical Multiwalled Carbon Nanotube Carpet to a Graphene Nanoribbon Carpet and Its Use in Supercapacitors. *ACS Nano* **2013**, *7*, 5151–5159.
- Lin, J.; Zhang, C.; Yan, Z.; Zhu, Y.; Peng, Z.; Hauge, R. H.; Natelson, D.; Tour, J. M. 3-Dimensional Graphene Carbon Nanotube Carpet-Based Microsupercapacitors with High Electrochemical Performance. *Nano Lett.* **2013**, *13*, 72–78.
- Liu, Z. W.; Peng, F.; Wang, H. J.; Yu, H.; Zheng, W. X.; Yang, J. Phosphorus-Doped Graphite Layers with High Electrocatalytic Activity for the O<sub>2</sub> Reduction in an Alkaline Medium. *Angew. Chem.* **2011**, *123*, 3315–3319.
- Yang, Z.; Yao, Z.; Li, G.; Fang, G.; Nie, H.; Liu, Z.; Zhou, X.; Chen, X. A.; Huang, S. Sulfur-Doped Graphene as an Efficient Metal-Free Cathode Catalyst for Oxygen Reduction. *ACS Nano* **2011**, *6*, 205–211.
- Wu, Z. S.; Winter, A.; Chen, L.; Sun, Y.; Turchanin, A.; Feng, X.; Müllen, K. Three-Dimensional Nitrogen and Boron Codoped Graphene for High-Performance All-Solid-State Supercapacitors. *Adv. Mater.* **2012**, *24*, 5130–5135.
- Fujisawa, K.; Cruz-Silva, R.; Yang, K.-S.; Kim, Y. A.; Hayashi, T.; Endo, M.; Terrones, M.; Dresselhaus, M. S. Importance of Open, Heteroatom-Decorated Edges in Chemically Doped Graphene for Supercapacitor Applications. *J. Mater. Chem. A* **2014**, *2*, 9532–9540.
- Wu, Z. S.; Parvez, K.; Winter, A.; Vieker, H.; Liu, X.; Han, S.; Turchanin, A.; Feng, X.; Müllen, K. Layer-by-Layer Assembled Heteroatom-Doped Graphene Films with Ultrahigh Volumetric Capacitance and Rate Capability for Micro-supercapacitors. *Adv. Mater.* **2014**, *26*, 4552–4558.
- Zuo, Z.; Jiang, Z.; Manthiram, A. Porous B-Doped Graphene Inspired by Fried-Ice for Supercapacitors and Metal-Free Catalysts. *J. Mater. Chem. A* **2013**, *1*, 13476–13483.
- Han, J.; Zhang, L. L.; Lee, S.; Oh, J.; Lee, K.-S.; Potts, J. R.; Ji, J.; Zhao, X.; Ruoff, R. S.; Park, S. Generation of B-Doped Graphene Nanoplatelets Using a Solution Process and Their Supercapacitor Applications. *ACS Nano* **2012**, *7*, 19–26.
- Niu, L.; Li, Z.; Hong, W.; Sun, J.; Wang, Z.; Ma, L.; Wang, J.; Yang, S. Pyrolytic Synthesis of Boron-Doped Graphene and Its Application as Electrode Material for Supercapacitors. *Electrochim. Acta* **2013**, *108*, 666–673.
- Wang, D.-W.; Li, F.; Chen, Z.-G.; Lu, G. Q.; Cheng, H.-M. Synthesis and Electrochemical Property of Boron-Doped Mesoporous Carbon in Supercapacitor. *Chem. Mater.* **2008**, *20*, 7195–7200.
- Shiraishi, S.; Kibe, M.; Yokoyama, T.; Kurihara, H.; Patel, N.; Oya, A.; Kaburagi, Y.; Hishiyama, Y. Electric Double Layer Capacitance of Multi-walled Carbon Nanotubes and B-Doping Effect. *Appl. Phys. A: Mater. Sci. Process.* **2006**, *82*, 585–591.
- Kwon, T.; Nishihara, H.; Itoi, H.; Yang, Q. H.; Kyotani, T. Enhancement Mechanism of Electrochemical Capacitance in Nitrogen-/Boron-Doped Carbons with Uniform Straight Nanochannels. *Langmuir* **2009**, *25*, 11961–11968.
- Lin, J.; Peng, Z.; Liu, Y.; Ye, R.; Samuel, E. L.; Ruiz-Zepeda, F.; Yacaman, M. J.; Jakobson, B. I.; Tour, J. M. Laser-Induced Porous Graphene Films from Commercial Polymers. *Nat. Commun.* **2014**, *5*, 5714.
- Peng, Z.; Lin, J.; Ye, R.; Samuel, E. L. G.; Tour, J. M. Laser Induced Graphene for Stackable, Flexible Supercapacitors. *ACS Appl. Mater. Interfaces* **2015**, *7*, 3414–3419.
- Lin, T.; Huang, F.; Liang, J.; Wang, Y. A Facile Preparation Route for Boron-Doped Graphene, and Its CdTe Solar Cell Application. *Energy Environ. Sci.* **2011**, *4*, 862–865.
- Palnitkar, U.; Kashid, R. V.; More, M. A.; Joag, D. S.; Panchakarla, L.; Rao, C. Remarkably Low Turn-on Field Emission in Undoped, Nitrogen-Doped, and Boron-Doped Graphene. *Appl. Phys. Lett.* **2010**, *97*, 063102.
- Wu, Z.-S.; Ren, W.; Xu, L.; Li, F.; Cheng, H.-M. Doped Graphene Sheets as Anode Materials with Superhigh Rate and Large Capacity for Lithium Ion Batteries. *ACS Nano* **2011**, *5*, 5463–5471.
- Unsal, E.; Cakmak, M. Real-Time Characterization of Physical Changes in Polyimide Film Formation: From Casting to Imidization. *Macromolecules* **2013**, *46*, 8616–8627.

41. Nohara, L. B.; Costa, M. L.; Alves, M. A.; Takahashi, M. F. K.; Nohara, E. L.; Rezende, M. C. Processing of High Performance Composites Based on Peek by Aqueous Suspension Prepregging. *Mater. Res.* **2010**, *13*, 245–252.
42. Lee, S. W.; Gallant, B. M.; Byon, H. R.; Hammond, P. T.; Shao-Horn, Y. Nanostructured Carbon-Based Electrodes: Bridging the Gap between Thin-Film Lithium-Ion Batteries and Electrochemical Capacitors. *Energy Environ. Sci.* **2011**, *4*, 1972–1985.
43. Dimiev, A. M.; Ceriotti, G.; Behabtu, N.; Zakhidov, D.; Pasquali, M.; Saito, R.; Tour, J. M. Direct Real-Time Monitoring of Stage Transitions in Graphite Intercalation Compounds. *ACS Nano* **2013**, *7*, 2773–2780.
44. Ferrari, A.; Meyer, J.; Scardaci, V.; Casiraghi, C.; Lazzeri, M.; Mauri, F.; Piscanec, S.; Jiang, D.; Novoselov, K.; Roth, S. Raman Spectrum of Graphene and Graphene Layers. *Phys. Rev. Lett.* **2006**, *97*, 187401.
45. Ferrari, A. C. Raman Spectroscopy of Graphene and Graphite: Disorder, Electron–Phonon Coupling, Doping and Nonadiabatic Effects. *Solid State Commun.* **2007**, *143*, 47–57.
46. Dong, X.; Su, C.-Y.; Zhang, W.; Zhao, J.; Ling, Q.; Huang, W.; Chen, P.; Li, L.-J. Ultra-large Single-Layer Graphene Obtained from Solution Chemical Reduction and Its Electrical Properties. *Phys. Chem. Chem. Phys.* **2010**, *12*, 2164–2169.
47. Bagri, A.; Mattevi, C.; Acik, M.; Chabal, Y. J.; Chhowalla, M.; Shenoy, V. B. Structural Evolution during the Reduction of Chemically Derived Graphene Oxide. *Nat. Chem.* **2010**, *2*, 581–587.
48. Sheng, Z.-H.; Gao, H.-L.; Bao, W.-J.; Wang, F.-B.; Xia, X.-H. Synthesis of Boron Doped Graphene for Oxygen Reduction Reaction in Fuel Cells. *J. Mater. Chem.* **2012**, *22*, 390.
49. Vishwakarma, P. N.; Subramanyam, S. V. Hopping Conduction in Boron Doped Amorphous Carbon Films. *J. Appl. Phys.* **2006**, *100*, 113702.
50. Beidaghi, M.; Wang, C. Micro-supercapacitors Based on Interdigital Electrodes of Reduced Graphene Oxide and Carbon Nanotube Composites with Ultrahigh Power Handling Performance. *Adv. Funct. Mater.* **2012**, *22*, 4501–4510.
51. Wu, Z. S.; Parvez, K.; Feng, X.; Müllen, K. Graphene-Based In-Plane Micro-supercapacitors with High Power and Energy Densities. *Nat. Commun.* **2013**, *4*, 2487.
52. Gao, W.; Singh, N.; Song, L.; Liu, Z.; Reddy, A. L. M.; Ci, L.; Vajtai, R.; Zhang, Q.; Wei, B.; Ajayan, P. M. Direct Laser Writing of Micro-supercapacitors on Hydrated Graphite Oxide Films. *Nat. Nanotechnol.* **2011**, *6*, 496–500.
53. Meng, Q.; Wu, H.; Meng, Y.; Xie, K.; Wei, Z.; Guo, Z. High-Performance All-Carbon Yarn Micro-supercapacitor for an Integrated Energy System. *Adv. Mater.* **2014**, *26*, 4100–4106.